UNIVERSITY OF HELSINKI REPORT SERIES IN PHYSICS

HU-P-D186

Computer simulation of multi-elemental fusion reactor materials

Katharina Vörtler

Division of Materials Physics
Department of Physics
Faculty of Science
University of Helsinki
Helsinki, Finland

ACADEMIC DISSERTATION

To be presented, with the permission of the Faculty of Science of the University of Helsinki, for public criticism in the Auditorium D101 of the Department of Physical Sciences (Physicum), on November 25th, 2011, at 12 o'clock noon.

HELSINKI 2011

ISBN 978-952-10-7064-8 (printed version)
ISSN 0356-0961
Helsinki 2011
Helsinki University Printing House (Unigrafia)

ISBN 978-952-10-7065-5 (PDF version)
http://ethesis.helsinki.fi/
Helsinki 2011
Electronic Publications @ University of Helsinki (Helsingin yliopiston verkkojulkaisut)

Katharina Vörtler **Computer simulation of multi-elemental fusion reactor materials**, University of Helsinki, 2011, 40 p.+appendices, University of Helsinki Report Series in Physics, HU-P-D186, ISSN 0356-0961, ISBN 978-952-10-7064-8 (printed version), ISBN 978-952-10-7065-5 (PDF version)

Classification (INSPEC): A2852F, A6180, A7920N
Keywords (INSPEC): fusion reactor materials, molecular dynamics, interatomic potentials, plasma-wall interactions, radiation damage, sputtering

ABSTRACT

Thermonuclear fusion is a sustainable energy solution, in which energy is produced using similar processes as in the sun. In this technology hydrogen isotopes are fused to gain energy and consequently to produce electricity. In a fusion reactor hydrogen isotopes are confined by magnetic fields as ionized gas, the plasma. Since the core plasma is millions of degrees hot, there are special needs for the plasma-facing materials. Moreover, in the plasma the fusion of hydrogen isotopes leads to the production of high energetic neutrons which sets demanding abilities for the structural materials of the reactor. This thesis investigates the irradiation response of materials to be used in future fusion reactors.

Interactions of the plasma with the reactor wall leads to the removal of surface atoms, migration of them, and formation of co-deposited layers such as tungsten carbide. Sputtering of tungsten carbide and deuterium trapping in tungsten carbide was investigated in this thesis. As the second topic the primary interaction of the neutrons in the structural material steel was examined. As model materials for steel iron chromium and iron nickel were used.

This study was performed theoretically by the means of computer simulations on the atomic level. In contrast to previous studies in the field, in which simulations were limited to pure elements, in this work more complex materials were used, *i.e.* they were multi-elemental including two or more atom species.

The results of this thesis are in the microscale. One of the results is a catalogue of atom species, which were removed from tungsten carbide by the plasma. Another result is *e.g.* the atomic distributions of defects in iron chromium caused by the energetic neutrons. These microscopic results are used in data bases for multiscale modelling of fusion reactor materials, which has the aim to explain the macroscopic degradation in the materials. This thesis is therefore a relevant contribution to investigate the connection of microscopic and macroscopic radiation effects, which is one objective in fusion reactor materials research.

Contents

1 INTRODUCTION

One part of facing the social, environmental, and economical challenges of the 21st century is the development of new technologies that provide *sustainable* energy. One of the technologies fulfilling the latter criterion is the energy production by thermonuclear fusion [1]. Assuming that fusion is technically and commercially feasible, it will provide energy on a large scale, produce no CO_2 emissions, have an almost limitless fuel supply, and will not require long-time storage of radioactive waste.

So far, only experimental fusion devices are existing. The largest one is the Joined European Torus (JET) in the UK. Currently, most efforts in fusion research are aimed towards the International Thermonuclear Reactor (ITER), which is shown in Fig. 1. The reactor is currently under construction in France, and its first operation is scheduled for 2019. The ITER project has the goal to demonstrate the feasibility of the technology and is considered to be the bridge towards the first demonstration power plant DEMO, aimed at making fusion commercially applicable [2].

One of the main problems in fusion research is to find suitable materials for the reactors that (i) withstand the extreme conditions in the reactors and (ii) produce only a limited amount of radioactive isotopes. Computer simulations are needed to obtain a theoretical understanding of the processes involved, and therefore help the experimental and engineering approaches for developing more advanced materials.

Previously, atomistic simulation studies of radiation effects in fusion reactor materials were limited mostly to pure elements [3–6]. Moreover, the time scales and system size were small due to restrictions in computer power. The aim of the present thesis is to use improved interaction models, which have become available only recently, to investigate radiation effects in multi-elemental materials for applications in future fusion reactors. Moreover, larger systems and longer simulation times are considered. In this thesis an interaction model for Fe-Ni is modified and applied to simulate the primary radiation damage by displacement cascades. The multi-elemental effects of Cr or Ni in Fe matrices induced by cascades on the defect production and ordering are investigated. Furthermore, the sputtering and blistering of tungsten carbide (WC) by the deuterium plasma is studied. The present work is in close collaboration with multiscale modelling research of fusion reactor materials on the European level.

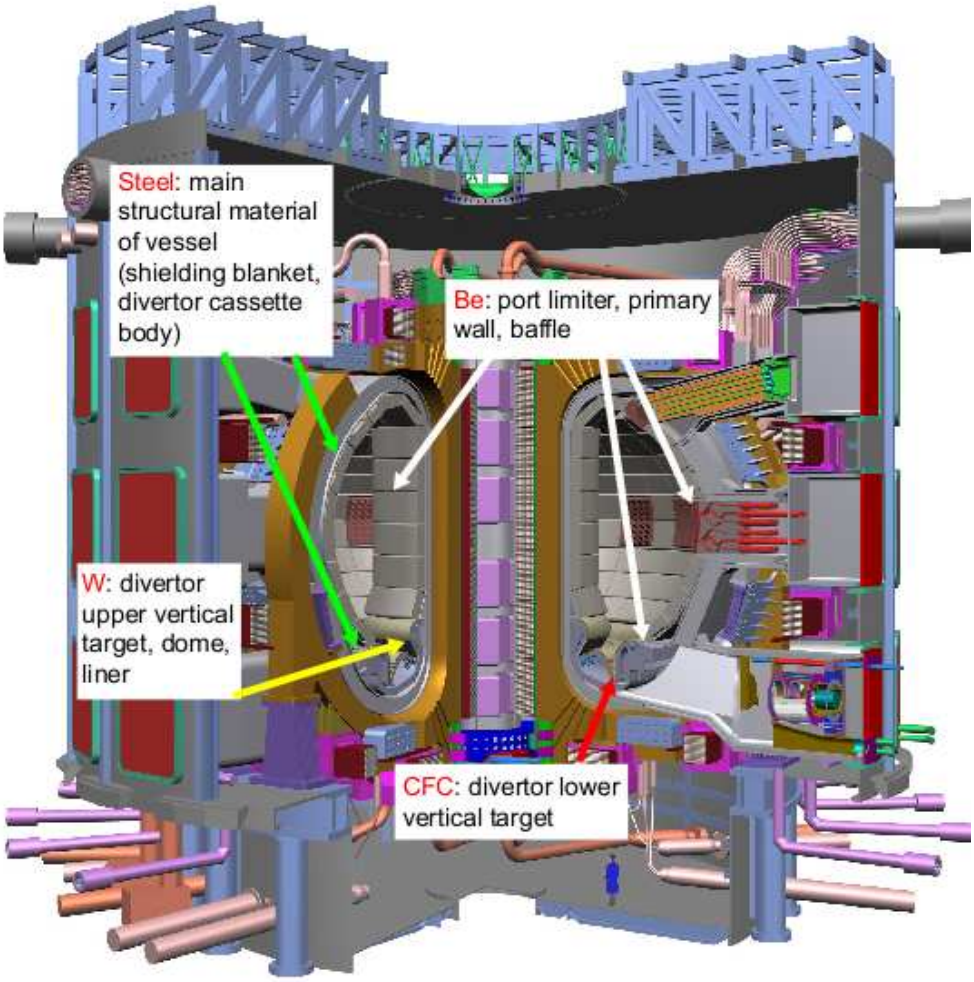

Figure 1: The concept design of the ITER tokamak reactor pointing out the main structural and plasma-facing materials [7]. ITER means “the way” in Latin. The reactor has the objective to produce more power than it consumes ($Q > 5$, where the *power amplification* Q is the ratio between electrical output and input), with a fusion power of 500 MW [7].

2 PURPOSE AND STRUCTURE OF THIS STUDY

The purpose of this thesis was to increase knowledge on the following two challenges in fusion reactor materials research: (i) the interaction of the plasma with the reactor wall and (ii) the damage production by neutron scattering in the structural materials of the reactor. The work was done computationally contributing towards the European modelling projects by the European Fusion Development Agreement (EFDA) [2] and the EURATOM 7th framework programme, under Grant Agreement Number 212175 (Getmat project) [8].

This thesis consists of five original publications that are referred to in in bold numerals and are given in the appendix. Background to fusion and reactor materials is summarized in section 3, the methodology is described in section 4, and the main results are reviewed in sections 5 and 6.

2.1 Summaries of the original publications

Publications **I** and **II** deal with plasma-wall interactions on WC. Molecular dynamics (MD) and dynamic binary collision approximation (BCA) simulations of cumulative deuterium (D) cobombardment with C, W, He, Ne or Ar impurities on WC were performed in the energy range 100 to 300 eV. The effect of the plasma impurities on sputtering was considered in **I**, changes in the crystal structure and D trapping and re-emission in **II**.

Research on the primary neutron radiation induced damage was performed in publications **III-V**. Displacement cascades in Fe-Cr and Fe-Ni alloys were studied using molecular dynamics simulation. Before simulating cascades in Fe-Ni, the interaction model for Fe-Ni was modified for cascade conditions in **V**. Single cascades were investigated in body-centered cubical (bcc) Fe-5%Cr and Fe-15%C in **III** and **IV**, and in face-centered cubical (fcc) Fe-Ni alloys in **V**. The accumulation of cascades in Fe-Ni and Fe-Cr was studied in **V**. The effect of Cr or Ni on the primary defect production by a cascade in Fe was studied in **III-V**, furthermore changes in the Cr or Ni ordering in the Fe matrices were examined in **III** and **V**.

Publication I: The effect of plasma impurities on the sputtering of tungsten carbide,
K. Vörtler, C. Björkas, and K. Nordlund, *Journal of Physics: Condensed Matter* **23**, 085002 (2011).

MD sputtering yields obtained at low fluences were compared to steady state dynamic binary collision approximation yields. During bombardment single C atom sputtering was preferentially observed. Significant W_xC_y molecule sputtering was detected, and the molecule sputtering mechanism was found to be of physical origin.

Publication II: Molecular dynamics simulations of deuterium trapping and re-emission in tungsten carbide,
K. Vörtler and K. Nordlund, *Journal of Physical Chemistry C* **114**, 5382 (2010).

During the D bombardment, the WC sample surface changed from crystalline to amorphous. Deuterium was trapped in the sample, followed by D_2 accumulation into bubbles which led in some cases to a "blistering"-like effect.

Publication III: The effect of Cr concentration on radiation damage in Fe-Cr alloys,
K. Vörtler, C. Björkas, D. Terentyev, L. Malerba, and K. Nordlund, *Journal of Nuclear Materials* **382**, 24 (2008).

The average number of surviving Frenkel pairs and the fraction of vacancies and self-interstitials in clusters was found to be approximately the same in pure Fe and random Fe-Cr alloys (regardless of Cr concentration). A noticeable effect of the presence of Cr in the Fe matrix was only observed in the enrichment of self-interstitials by Cr in Fe-5%Cr. The calculated change in the short range order parameter showed that Fe-5%Cr tends towards ordering (negative short range order parameter) and Fe-15%Cr towards segregation (positive short range order parameter) of Cr atoms.

Publication IV: Primary radiation damage in bcc Fe and Fe-Cr crystals containing dislocation loops,
D. Terentyev, K. Vörtler, C. Björkas, K. Nordlund, and L. Malerba, *Journal of Nuclear Materials*, **417**, 1063 (2011).

MD simulations of single cascades in Fe-Cr alloys containing 5 to 15% Cr were performed. The analysis of the size distribution of self-interstitial clusters was studied, finding no statistically significant influence of Cr as compared to Fe.

Publication V: The effect of prolonged irradiation on defect production and ordering in Fe-Cr and Fe-Ni alloys,
K. Vörtler, N. Juslin, G. Bonny, L. Malerba, and K. Nordlund, *Journal of Physics: Condensed Matter* **23**, 355007 (2011).

Accumulation of cascades were simulated to study the difference between fcc and bcc lattices, as well as initially ordered and random crystals. With increasing number of cascades a saturation of Frenkel pairs in the bcc alloys was observed. In fcc Fe-Ni, on the contrary, a continuous accumulation of defects was seen: the growth of stacking-fault tetrahedra and a larger number of self-interstitial atom clusters were seen in contrast to bcc alloys. For all simulations the defect clusters and the short

range order parameter were analyzed. The modification of the repulsive part of the Fe-Ni interaction potential is also reported, which was needed to study the non-equilibrium processes.

2.2 Author's contribution

The author of this thesis carried out all the work for **I** and **II**. The displacement cascade simulations in Fe-5%Cr and Fe-15%Cr and related analysis in **III** and **IV** were done by the author (besides the loop analysis in **IV**, which was done by D. Terentyev). All work in **V** was done by the author, besides the Ni–Ni pair potential modification and part of the displacement threshold calculations given in the Appendix of the publication. The author wrote part of the text of **III** and **IV**, and all text of publications **I**, **II**, and **V**. She was the corresponding author in all publications.

3 MULTI-ELEMENTAL FUSION REACTOR MATERIALS

3.1 Thermonuclear fusion

The source of fusion energy is the binding energy of the atom's nucleus. The nucleus consist of protons with positive charge and neutrons of similar mass but no charge. Strong nuclear forces hold the nucleus together, with electrons located around it to balance the charge of the protons. By fusing light nuclei like hydrogen, energy is gained due to the change in the nucleus' mass.

The strong repulsion of nuclei can be overcome by colliding them at high kinetic energies, which are achieved *e.g.* in a plasma, where electrons and ions are separated. Since a plasma is electrically conductive, it is influenced by electric and magnetic fields. The latter is used in a tokamak fusion reactor (see next section). A fusion reaction triggered this way is called *thermonuclear fusion* [1]. Of the light elements the fusion reaction between deuterium and tritium,

$$D + T \rightarrow {}^4He + n + 17.58\,\mathrm{MeV}, \tag{1}$$

gives the largest energy at the lowest plasma temperatures, where the neutron n carries 80% and the helium ${}^4He$ 20% of the gained energy. This reaction is by far the easiest to accomplish [9], and will be used in future fusion power plants, although it has the disadvantages of tritium being radioactive and the internal reactor parts being activated by the neutrons.

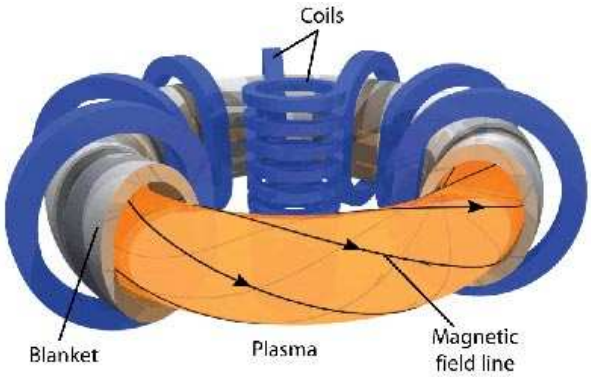

Figure 2: In a tokamak the plasma is confined in a twisted toroidal magnetic field which is produced by the two sets of coils [2]. The figure also shows the blanket.

3.2 Tokamak fusion reactors

A *tokamak* is a toroidal plasma confinement system using magnetic fields. Figure 2 illustrates the tokamak principle: the superposition of two sets of coils confine the plasma in a twisted toroidal magnetic field.

The reactor vessel of a tokamak is vacuum-proof to prevent the penetration of air from the outside and the leakage of the fuel from the inside. The *blanket* (Fig. 2) covers the first wall. It is especially significant in future fusion reactors, where it acts as a heat exchanger to produce electricity. Due to the fast neutrons the material selection of the blanket is crucial (see section 3.4), since it also shields the outer components of the reactor. Moreover, in the blanket fast neutrons produce the tritium fuel with the help of lithium [1, 9].

The magnetic field in the vessel is shaped in such a way, that after the last closed magnetic surface, the *separatrix*, only open surfaces follow, guiding the particles to the divertor. The separatrix acts as a magnetic limiter, separating the confined plasma from the wall. The *divertor* is situated at the lower part of the vacuum vessel in Fig. 1. It consists of special cooled plates, where the high particle flux leads to a high gas pressure. This leads to the neutralization of particles, and the neutral gas is pumped off. Due to the imperfect confinement, the plasma loses continuously particles. The fuel is refilled by *e.g.* puffing frozen pellets of deuterium and tritium into the vessel [9].

3.3 Plasma-wall interactions on mixed materials

In a fusion reactor the plasma is not perfectly confined by the magnetic fields. Ions from the plasma will therefore reach the reactor walls, the plasma-facing materials (PFMs). In ITER, the PFMs will

consist of W, C, and Be [7] (Fig. 1). WC will not be used directly as wall material, however, due to erosion and redeposition effects it will form as mixed material in films on the divertor plates [10, 11]. Recently, there has been a growing interest in studying of mixed materials since their properties substantially differ from the pure elements.

In publications **I** and **II** the interactions between the plasma and the PFMs were studied, which is relevant for the following reasons: (i) Chemical changes in the wall material by hydrogen isotope and impurity bombardment determine among other effects how fast the wall material degrades during reactor operation. (ii) Eroded wall material increases the impurity level of the plasma; the eroded particles are not fully ionized and therefore reduce the energy of the plasma by radiation. (iii) D re-emission from the wall material to the plasma also affects the recycling of unburned fuel. (iv) The T retention in the wall material is, apart from degrading the material's properties, a crucial factor for ITER: the retention of the hydrogen isotope tritium in the reactor components is a safety criterion for operation. The feasibility of future commercial fusion reactors depend on all the four above mentioned facts.

One of the interactions of the plasma with the PFMs is *sputtering*, which was studied in publication **I**. Sputtering describes the removal of surface atoms caused by energetic particle bombardment [12]. The sputtering yield Y of the removed surface atoms is defined

$$Y = \frac{n_{sput}}{n_{impacts}}, \tag{2}$$

where n_{sput} is the number of sputtered atoms and $n_{impacts}$ the number of impinging ions. Generally two sputtering phenomena are distinguished: physical and chemical sputtering. Physical sputtering is caused by the momentum transfer of the bombarded ions to the surface atoms. Depending on the mass and energy of the impinging particles also dimers [13] and clusters [14] may be found among the sputtered particles. In chemical sputtering, chemical reactions between the impinging particles and the material cause molecule sputtering. The threshold energy for chemical sputtering is below the physical one [12]. Bond-breaking by light ions in the swift chemical sputtering process [15] also leads to molecule emission. Preferential sputtering of one atom species is generally observed in multi-elemental systems. The reason is that the surface binding energies are usually different for each atom species.

Sputtering of pure C and hydrocarbon surfaces by low energy hydrogen isotopes has been studied widely [15–20], also including noble gas bombardment [21, 22]. However, little attention has been drawn to the mixed material WC. Moreover, previous research in the field was mostly limited to high ion energies due to experimental [23–26] and computational [27] limitations. Only one work of sputtering by D bombardment on WC surfaces previously to publication **I** was conducted using

MD simulations [3, 28]. The work by Träskelin *et al.* [28] used a realistic interaction model allowing chemical effects to be described. In publications **I** and **II** issues that were previously not considered by atomistic simulations, are addressed. These topics are the effect of plasma impurities on the sputtering yields, and the structural changes in the WC sample due to the ion bombardment, whose results are summarized in sections 5.1 and 5.2.

Once the hydrogen isotopes ordinating from the plasma have reached the reactor wall, hydrogen accumulation in the PFMs degrades the wall since the trapped hydrogen can form voids, bubbles, and blisters [29]. Energetic D implantation into W leads to the formation of blisters on its surface [30]. Figure 3 shows blisters of micro size by grazing-incidence microscopy [31]. Blisters are also observed if carbon is present in the W matrix [32–34]. A *blister* is a void or bubble close to the sample surface [29]. In this thesis as *blistering* is referred a rupture in the sample leading to an expanding void. This process is also sometimes called *flaking* or *exfoliation*. The mechanism of hydrogen-induced blister formation in W is not yet fully understood, although both experiments [32] and FEM simulations [31] have been performed to tackle this problem. Recent experiments indicate that diffusion processes of D in W are responsible for forming blisters [34, 35].

A comparison of experimental [36–38] and realistic simulation data of deuterium retention and re-emission in WC is lacking. The reasons for this are simulation difficulties arising due to the experimental value of the D flux, which restricts the system size and therefore the realization of realistic simulations. Therefore, a direct understanding of the trapping and re-emission mechanisms of D in WC has not yet been obtained. The purpose of publication **II** was to investigate deuterium trapping and re-emission on WC surfaces, whose most striking result was a blistering-like effect that is described in section 5.2.

3.4 Neutron induced displacement damage in structural materials

The neutron absorption in the structural materials is a challenge: the materials have to tolerate the high energetic neutrons (14 MeV) and produce only a small amount of radioactive waste [7]. One goal in fusion research is the design of low activation materials *e.g.* advanced reduced activation ferritic/martensitic (RAFM) steels. The aim is to limit the half-lives of most radioisotopes to 10 years [2].

Steel consists mostly of Fe, and depending on application some weight percentage Cr for *e.g.* stainless and/or Ni for *e.g.* duplex steels. Another alloying elements is C. For applications as structural material in a fusion reactor, steels with Cr concentrations of 5 to 15% are of most interest. In publications **III-V**

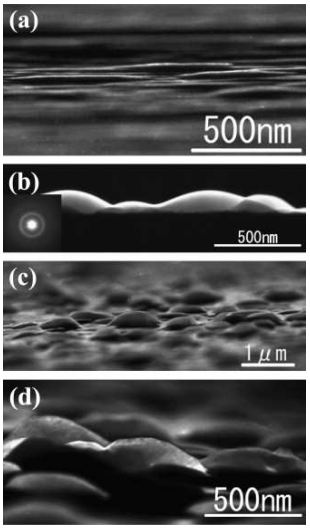

Figure 3: Blisters in W after D irradiation observed by grazing-incidence microscopy [31]. This figure is reproduced with permission from Elsevier.

multi-elemental model materials for steel were considered. Fe-Cr for bcc and Fe-Ni for fcc structured steels were used to study their basic features under the first stage of neutron irradiation.

Radiation damage by energetic particles (neutrons, electrons, ions) in materials leads to changes in the material properties. The scattering of these particles induces atomic collisions that can produce an avalanche of collisions at the atomic level. The latter processes are called *displacement*, or *collision cascades* and were investigated in publications **III-V**. In cascade simulations only the primary state of damage produced by the primary knock-on atom (PKA) is considered, which is independent of bombarding particle and mass [39]. The damage production by cascades have been experimentally (indirectly) observed in metals by field ion microscopy (FIM) [40, 41] and studied (directly) by means of computer simulations [42–46]. The theoretical concept goes back to Seeger [47] and Brinkman [39]. For ion impacts on surfaces as described in the previous section, surface cascades may result in the sputtering of surface atoms.

Cascades are processes of picoseconds and lead to microscopic effects *i.e.* points defects. Snapshots of a single cascade in Fe-5%Cr is illustrated in Fig. 4. A future fusion reactor will be operated over years, thus much longer time scales are present. Constant production of point defects by irradiation changes the macroscopic properties of a material, since defects are mobile and migrate at elevated temperatures. Migrating defects can lead to effects such as radiation-enhanced diffusion, segregation, and creep [45]. Moreover, additional dislocation loops can be created, raising the dislocation density of the material. In the structural materials of a fusion reactor the transmutation He present may diffuse into vacancy clusters, that can grow to voids, causing the material to swell up to tens of percents [48]. The prediction of those effects is essential, therefore the general objective in fusion materials research

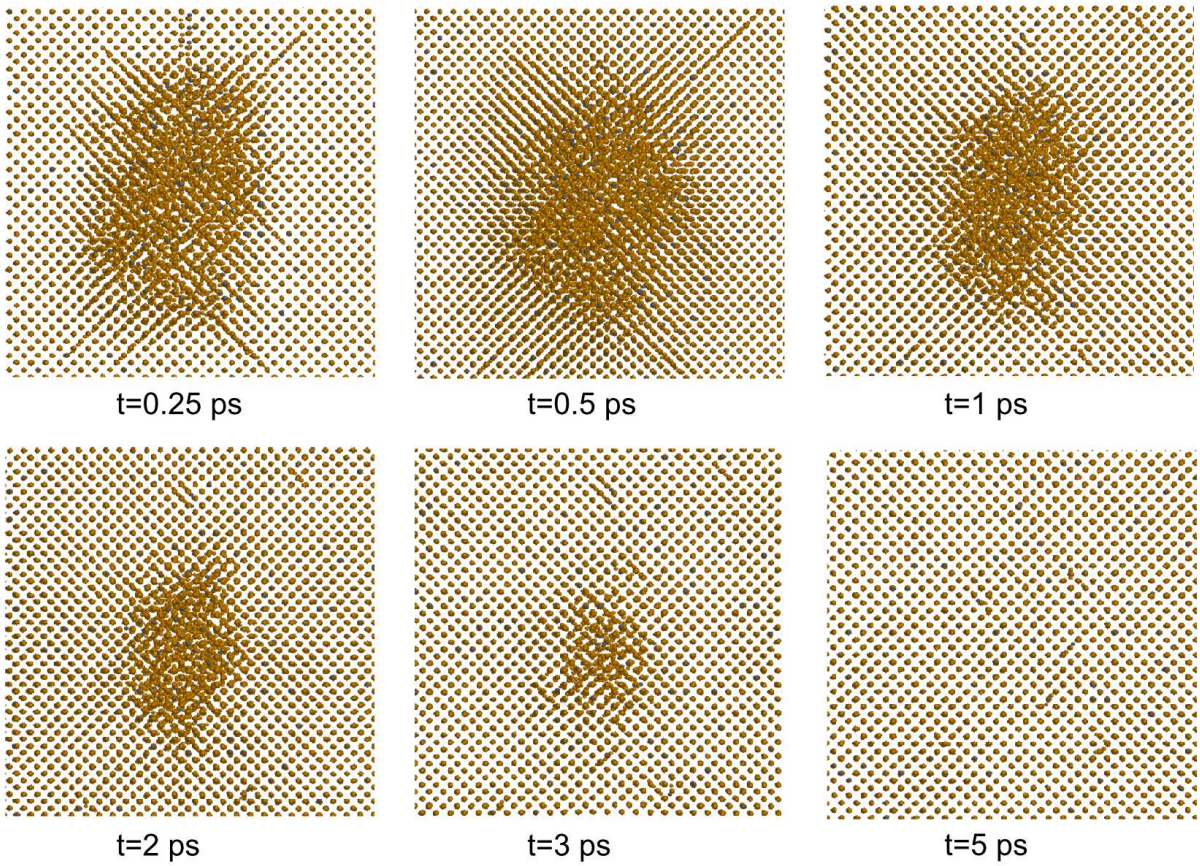

Figure 4: Snapshots of the time evolution from a single 5 keV cascade in Fe-5%Cr. Color code: orange/light gray spheres represent Fe, dark gray ones Cr. The figures show the projection of a full three-dimensional cell into a two-dimensional plane. The figures show part of the bulk simulation cell near its center where the cascade was initiated.

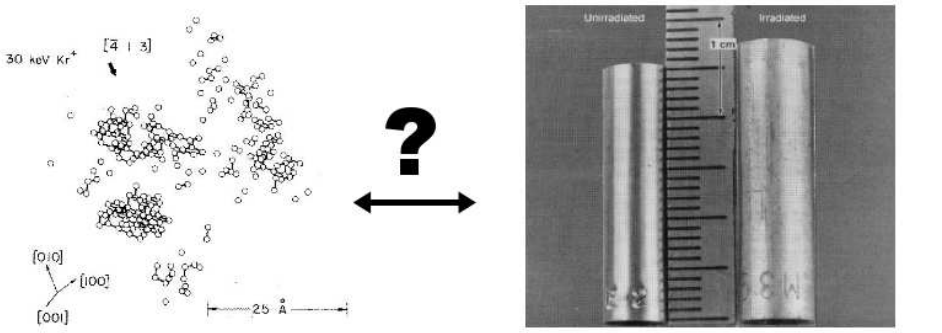

Microscopic effect: Field ion microscopy visualization of vacancy clusters created by a cascade in tungsten.

Macroscopic effect: Swelling of stainless steel after irradiation with neutrons.

Figure 5: The main question in the research of radiation damage in materials. How are microscopic [40] and macroscopic [49] effects connected? The figures are reproduced with permission from Taylor & Francis and Elsevier.

is to explore how microscopic and macroscopic radiation effects are connected (Fig. 5). The involved processes are very complex and no comprehensive understanding has yet been obtained. Multiscale modelling, with MD being one part of the frame, is undertaken to solve the problem.

The primary damage state of displacement cascades using MD was previously to publications **III-V** studied mostly in pure bcc iron [5, 50] and Fe-based systems [51–53]. In the Fe-Cr alloys mostly Fe-10%Cr was studied [5, 54–57], with the exception of the work by Wallenius *et al.* [58], that also considered Cr concentrations of 5 and 20%. Although different interatomic interaction models were used, it was concluded: (i) the presence of Cr hardly affects the number of formed Frenkel pairs (FPs) and their distribution in clusters as compared to pure Fe, and (ii) self-interstitial atoms (SIAs) and their clusters were observed to be enriched by Cr atoms. Publications **III-V** investigate the effect of Cr on the primary defect production and ordering induced by single and agglomerating cascades. The results are summarized in section 6.

For Fe-Ni alloys, an interaction model potential able to describe the ferritic and austenitic phases as well as the correct defect properties and phase stability has only recently become available, and was previously to publication **V** not yet adapted for cascade simulations [59]. The modification of the potential was done in **V** (see section 4.4) before using it in cascade simulations, whose results are reviewed in section 6.

3.5 Theoretical background on radiation damage in solids

Analytically, the penetration of energetic particles into solid materials is described by solving the two-body central force scattering problem [45, 60]. The scattering angle between the particle (projectile) and the collision atom (center-of-mass frame) is calculated as

$$\theta = \pi - 2\int_0^{1/\rho} \left(\frac{1}{p^2}\left[1 - \frac{V(u)}{E_1}\frac{m_1+m_2}{m_2}\right] - u^2 \right)^{-1/2} \mathrm{d}u, \tag{3}$$

where $V(u)$ is the interatomic potential of the collision partners, E_1 the initial projectile energy (laboratory frame), $u = 1/r$ with r being the distance separating the collision partners. The closest distance of r is ρ. The distance between target atom and the asymptote of the projectile is p, which is related to the differential (nuclear stopping) cross section (the likelihood of the interaction of two scattering particles) $\mathrm{d}\sigma = 2\pi p \mathrm{d}p$. Once the scattering angle is known, the trajectories of the energetic particles can be calculated.

The energy loss of a moving ion or recoil does not only depend on elastic collisions. The energy stopping power

$$\frac{\mathrm{d}E}{\mathrm{d}x} = \left(\frac{\mathrm{d}E}{\mathrm{d}x}\right)_n + \left(\frac{\mathrm{d}E}{\mathrm{d}x}\right)_{el} \tag{4}$$

depends not only on nuclear (elastic scattering) n, but also on the excitation of electrons el, since the electrons of the target atom can get excited and thus cause energy loss [45].

Solving the scattering integral is used in BCA calculations (section 4.1). It is suitable when two-body *i.e.* binary collisions are a sufficient description. In MD simulations (section 4.2) a different approach is used: the collisions are treated as N-body problem, the scattering integral is not solved, and no trajectories are calculated. In both MD and BCA simulations electron stopping models may be applied (section 4.1 and 4.2).

Applying conservation laws for energy and momentum one obtains a distribution of the energy E_{kin}, that an irradiating particle can give to a PKA

$$E_{kin} = \frac{4m_1m_2}{(m_1+m_2)^2} E_1 \sin^2\frac{\theta}{2} = E_{kin}^{max}\sin^2\frac{\theta}{2}, \tag{5}$$

where m_1 and E_1 are mass and energy of the irradiating particle, m_2 the mass of the PKA, E_{kin}^{max} the maximum PKA energy, and θ the resulting scattering angle in the center-of-mass frame. The consequence of Eq. 5 are maximum PKA energies of 1 MeV in Fe for the 14 MeV fusion neutrons.

4 METHODS

Length and time scales of cascades are too small for direct experimental observation, however, they can be modelled well by atomistic simulations. When choosing the simulation model, one has to compromise between realistic enough force description, system size, and time scale. In the following, the basic principles of dynamic binary collision approximation and classical molecular dynamics are described. The particular features of the codes, which were used in this thesis, are briefly characterized. Moreover, special emphasis is given to the MD interaction models, that were used in this thesis.

4.1 Dynamic binary collision approximation

In BCA simulations it is assumed that the collisions between the atoms can be approximated by elastic (binary) scattering as in Eq. 3. Conservation of energy is assumed: the elastic energy loss of the projectile/moving atom determines the energy transfered to the recoil atom. Due the assumptions in Eq. 3 the trajectories are asymptotic and the interaction potential is purely repulsive. The potential is usually a screened Coulomb potential of the form

$$V(r) = \frac{1}{4\pi\varepsilon_0}\frac{Z_1 Z_2}{r}\Phi(\frac{r}{a}), \tag{6}$$

where Z_1 and Z_2 are the charges of interaction nuclei, r the interatomic distance, and ε_0 the electric constant. Most commonly, the universal Ziegler-Biersack-Littmark (ZBL) [60] screening function

$$\Phi(x) = 0.1818e^{-3.2x} + 0.5099e^{-0.9423x} + 0.2802e^{-0.4028x} + 0.02817e^{-0.2016x}, \tag{7}$$

where $x = \frac{r}{a}$ is used with the screening length

$$a = \frac{0.8854a_0}{Z_1^{0.23} + Z_2^{0.23}}, \tag{8}$$

where a_0 is Bohr's radius.

The energy loss to electrons is treated separately as inelastic energy loss in analogy of the electronic stopping in Eq. 4. Usually, in BCA codes the atom collisions are treated sequentially until a minimum threshold energy is reached. The incident projectiles are followed in three-dimensional coordinates. A target surface layer atom is considered to be sputtered if its energy normal to the surface is larger than the surface binding energy [12].

SDTrimSP [61], which was used in publication **I**, is a dynamic BCA code specialized for describing sputtering in multi-elemental systems. As target composition an amorphous structure is employed, which is often called Monte Carlo program [12]. In dynamic BCA programs the target composition is updated during the bombarding process, which is needed in multi-elemental systems, when preferential sputtering of one atom type is present.

The advantage of BCA codes is its speed, which is four to five orders of magnitude faster than MD (next section) [12]. Problems with BCA arise whenever its assumptions are no longer sufficient, for example at low ion energies, in very dense materials, or when chemical effects play a role.

4.2 Classical molecular dynamics

The basic principle of classical MD is calculating the time evolution for a system of atoms. Newton's equations of motion are numerically solved over a short time interval dt

$$\frac{d}{\mathrm{d}t}(m_i\mathbf{v}_i) = \mathbf{F}_i = -\nabla V, \tag{9}$$

where m_i and $\mathbf{v}_i$ are the masses and velocities of the atoms, and $\mathbf{F}_i$ are the forces between them, which are determined by the interatomic potential energy function V. Thus, when knowing the forces between the atoms, one can derive the changes in the atom positions $\mathbf{r}_i$ using the relation

$$\frac{d\mathbf{r}_i}{\mathrm{d}t} = \mathbf{v}_i. \tag{10}$$

In the MD algorithm the atom positions and velocities are determined at each time step. In order to guarantee a realistic description of the system, two factors have to be considered. Firstly, the solution of Eq. 9 has to be numerically stable and therefore ensure energy conservation by using a suitable algorithm (e.g. the *Gear 5* algorithm [62]) with a time step Δt chosen small enough. Secondly, the force interactions between the atoms, *i.e.* the interatomic potential V in Eq. 9, have to be described as realistically as possible without slowing down the MD algorithm too much by their calculation.

PARCAS [63] is an MD code, which was used in all publications in this thesis and is specialized for simulating non-equilibrium processes *e.g.* cascades. It uses a variable time step [64], ensuring the accuracy of Eq. 9 when velocities and forces are high. The new time step Δt_{new} is determined by

$$\Delta t_{new} = \min\left(\frac{k_t}{v}, \frac{E_t}{Fv}, 1.1\Delta t_{old}, t_{max}\right), \tag{11}$$

where k_t and E_t are proportionality constants for velocity v and force F. The new time step Δt_{new} may not increase more than 10% in each step, and t_{max} is a maximum time step of *e.g.* 3 fs [65]. Moreover, to speed up the calculation of the neighboring atoms for the potential a linkcell method [66] is implemented [46].

In order to simulate virtually infinite systems, periodic boundary conditions [66] are used. They are employed in three dimensions for cascades in bulk materials in publications **III-V**, and in two dimensions for simulating ion bombardment on surfaces in publications **I** and **II**.

Initially, the simulation cell is equilibrated using Berendsen temperature and pressure control [67]. The temperature is coupled to an external heat bath by scaling the atom velocities by a factor

$$\lambda = \sqrt{1 + \frac{\Delta t}{\tau_T}\left(\frac{T_0}{T} - 1\right)}, \tag{12}$$

where T_0 is the desired temperature, T the temperature of the system, Δt the time step, and τ_T the time constant for the temperature control. Similarly, for coupling the pressure the atom positions are scaled by

$$\mu = \sqrt[3]{1 - \frac{\beta \Delta t}{\tau_P}(P_0 - P)}, \tag{13}$$

where τ_P is the time constant, β the isothermal compressibility of the system, P the pressure of the system, and P_0 the desired pressure [67]. During the simulation of non-equilibrium processes, the cell borders are coupled to a Berendsen heat bath mimicking the temperature flow to a larger system.

As in BCA, an electronic stopping power can be applied in analogy to the energy loss by electron-electron collisions and excitations (Eq. 4). It can be understood as a damping force in the equations of motion [45]. The most commonly applied electronic stopping model is the Ziegler-Biersack-Littmark (ZBL) stopping [60].

The main limitation of MD is its time step, which restricts the system size for cascades to a few million atoms (publications **III-V**). In low energy ion bombardment simulations, the system size is restricted to a few thousand atoms (publications **I** and **II**), since many ion impacts are consecutively performed. This results in orders of magnitude too high fluxes and too low fluences compared to experiments.

4.3 MD interatomic potentials for multi-elemental systems

Analytical interatomic interaction models describing the variation of the local chemical environment in multi-elemental system reasonably well compared to experimental and *ab initio* data can give a realistic description of physical processes in fusion reactor materials when applied in MD simulations. Since the solution of Eq. 9 is potential dependent, the outcome of an MD simulation is very sensitive to the applied potential. In general, potentials, describing the force interaction between atoms in a solid, depend on the interatomic distances and consist of attractive and repulsive terms due to like or different charges between nuclei and electrons at those distances. Although they are classical, their formalism is usually derived from quantum mechanical principles.

The potentials, which were used in publications **I** and **II**, are of the Tersoff-Brenner formalism. In **III-V** embedded atom model (EAM) potentials were applied. The potentials used in this thesis are briefly introduced in the following subsections.

4.3.1 Tersoff-Brenner-like: W-C-H system

A realistic potential for WC has to be able to describe the different character of W and C, *e.g.* the covalent bonding between C-C and C-W, and the metallic bonding between W-W. In the bond-order approach the strength of a single chemical bond is affected by the chemical environment including angularity being able to describe mixed covalent-metal systems [68]. The physical background is quantum mechanical and was derived by Abell [69] using linear combination of atomic orbitals (LCAO) based on chemical pseudopotential (CP) theory. He derived the following relation between energy and interatomic distance

$$E_b(G,q;r) \simeq Z(G)[qV_R(r) + p(G,q)V_A(r)], \tag{14}$$

where $Z(G)$ is the number of nearest neighbors, G the interaction topology, q the number of valence electrons per atom, and p the bond order. V_R and V_A are repulsive and attractive pair interactions. Furthermore, using tight-binding (TB), the bond-order

$$p(G,q) \propto Z^{-1/2}, \tag{15}$$

depends on the coordination number Z [69]. Using further assumptions Tersoff developed an analytical potential for silicon [70], and Brenner modified it for hydrocarbons [71]. Using the latter

formalism and the Albe notation [68], for the W-C-H system Juslin *et al.* [72] write the total energy as a sum over the individual bond energies

$$E = \sum_{i>j} f_{ij}^{c}(r_{ij}) \left[V_{ij}^{R}(r_{ij}) - \underbrace{\frac{b_{ij} + b_{ji}}{2}}_{\overline{b_{ij}}} V_{ij}^{A}(r_{ij}) \right], \tag{16}$$

where V^R and V^A are pair potential-like repulsive and attractive terms, f^c a cutoff-function (restricting the number of neighboring atoms), and $\overline{b_{ij}}$ the environment dependent bond-order term. The bond-order parameter b_{ij} includes the strong directional dependence of covalent bonds

$$b_{ij} = (1 + \chi_{ij})^{-1/2}, \tag{17}$$

where the χ function includes three-body contributions and angularity.

The potential functions were fitted to experimental and *ab initio* data. The elastic and structural properties of the bond-order potential compare well with experiment and density functional theory (DFT). The potential was explicitly designed to study hydrogen interactions in W-C systems [72].

4.3.2 EAM-like: Fe-Cr and Fe-Ni alloys

Embedded atom model potentials were derived in analogy to metallic bonding, where atoms are considered to be embedded in a sea of electrons [73]. Daw and Baskes derived the EAM *ansatz* by expressing the energy as a functional of the electron density (in a similar manner as in density functional theory)

$$E_{tot} = \sum_{i} F_i(\rho_i), \tag{18}$$

where F_i is the embedding energy, and ρ_i the electron density of an "impurity" at the atom site i neglecting the self-generated density [74]. In the EAM approach a correction term for pairwise short-range repulsion is added.

$$E_i = \frac{1}{2} \sum_{i,j} V_{i,j}(r_{ij}) + \sum_{i} F_i(\rho_i), \tag{19}$$

where $V(r_{ij})$ is a pairwise electrostatic interaction between core electrons depending on the distance between atoms $r_{r_{ij}}$. The electron density is $\rho_i = \sum_{i \neq j} \phi_j(r_{ij})$. The form in Eq. 19 was used by Bonny *et al.* in the potential set for the Fe-Ni system [59].

The EAM ansatz is widely used in metallic systems. It has been adapted, for example, in the Fe potential by Dudarev and Derlet [75], which takes into account magnetic properties, and by the two-band EAM Fe-Cr potential by Olsson *et al.* [76] by extending the embedding function F_i. In the latter one the extension of F_i was done in analogy to Ackland and Reed [77], by showing that for realistic description of the mixing energies in Fe-Cr the electron density of *s*- and *d*-band have to be included [76]. Consequently, the total energy for atom *i* is written

$$E_i = \frac{1}{2}\sum_{i,j} V_{i,j}(r_{ij}) + \sum_i F_i^d(\rho_i^d) + \sum_i F_i^s(\rho_i^s), \tag{20}$$

where the electron density of the *s*- and *d*-band are applied in the functional $F_i^b(\rho_i^b)$. The band functional is written

$$F_i(\rho_i) = A_1\sqrt{\rho_i} + A_2\rho_i^2 + A_3\rho_i^4, \tag{21}$$

where A_k parametrise the relative strength of the cohesive and repulsive forces. The first term on the right-hand side of Eq. 21 is linked to TB, the other two terms are arbitrary polynomials in line with Ackland *et al.* [78]. In the Fe-Ni potential [59] the functional in Eq. 21 is used in the Fe embedding function. The one for Ni has no analytical form and was derived by fitting [79].

EAM potential parameters are generally fitted to data obtained by *ab initio* calculations. For the Fe-Cr potential by Olsson *et al.* [76], two different data sets where used for fitting substitution and mixing energies. One set corresponds to data obtained using the Exact Muffin-Tin Orbital (EMTO) method [80], the other was calculated using the Projector Augmented Wave (PAW) method [81, 82].

The potentials for Fe-Cr and Fe-Ni describe point-defect properties, such as the stability and mobility of SIAs in different configurations, and thermodynamic properties of the alloy, for example the heat of mixing. The Fe-Ni potential describes the ferritic and austenitic phases.

4.4 Stiffening of Fe-Ni interatomic potential

Generally, MD potentials are constructed *i.e.* fitted describing equilibrium systems of solids. For describing high-energy collisions, the repulsive part of the equilibrium potential is modified (stiffened) to take into account the Coulomb interactions between nuclei at distances smaller than the equilibrium atomic distance r_0.

In publication **V** the repulsive parts of the EAM Fe-Ni and Ni-Ni potentials were stiffened using the corresponding universal ZBL repulsive potentials (Eq. 6). To do so, the ZBL repulsive potentials [60]

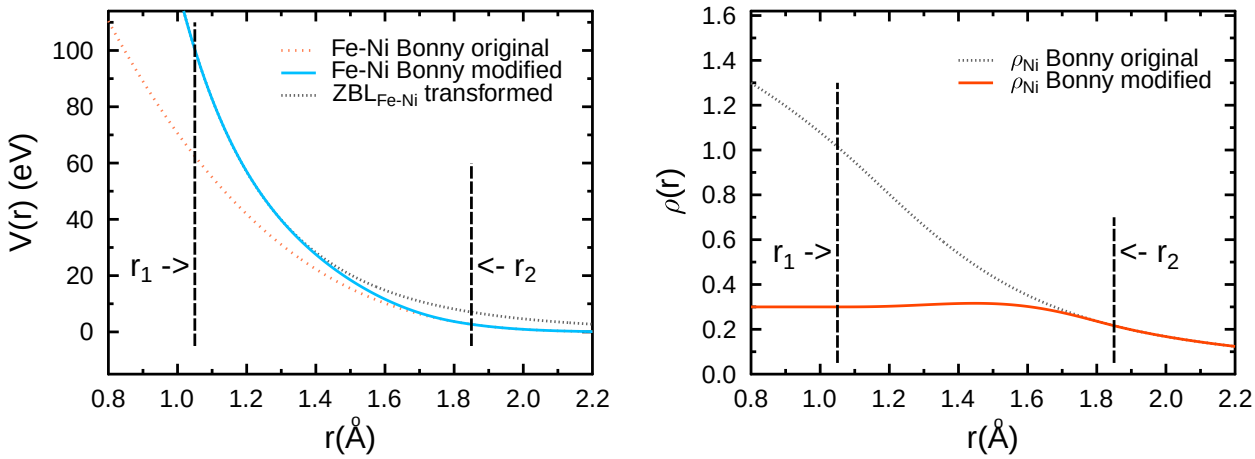

(a) (b)

Figure 6: Modified (a) Fe-Ni potential and (b) electron density ρ_{Ni}. The transformed ZBL repulsive potential (a) and the constant 0.3 (b) were fitted to the original functions by Bonny et al. [59] from the atomic distances r_1 to r_2. The electron density in (b) has arbitrary units. From publication **V**.

were first transformed as in [59] and lowered by 50 eV for Ni–Ni. The modified EAM pair potential was then constructed by taking the (transformed and possibly lowered) ZBL repulsive potential for atomic distances smaller than r_1, the equilibrium EAM pair potential for distances larger than r_2, and joining the two parts using the interpolating polynomial

$$p_{int} = a_0 r^5 + a_1 r^4 + a_2 r^3 + a_3 r^2 + a_4 r + a_5, \tag{22}$$

where a_n are the polynomial parameters.

In addition, the EAM electron density for Ni was modified to avoid a double representation of the repulsive interactions [83]. The modified Ni EAM electron density was set to $\rho_C^{Ni} = 0.3$ for distances smaller than r_1, the original (transformed) density for distances larger than r_2, and for values in between by a fitted polynomial of the form in Eq. 22. The modified Fe-Ni potential and electron density ρ_{Ni} is given in Fig. 6. The polynomial parameters are in published in **V**. To check the parameters, displacement threshold energies in the Fe-Ni system were calculated. They are given in **V** and are appropriate for cascade studies.

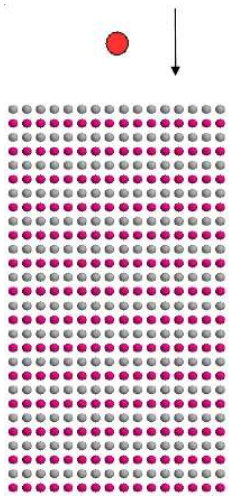

Figure 7: Simplified initial simulation set-up for bombardment simulations on crystalline WC. The red/gray ball represents the bombarding ion, magenta/dark gray W and light gray C atoms of the initial sample. The figure shows the projection of a full three-dimensional cell into a two-dimensional plane.

5 EFFECTS OF FUSION PLASMA ON WC

5.1 Sputtering

In publication **I** the effect of plasma impurities on the sputtering of WC surfaces was investigated. For that reason, cumulative bombardment of D with C, W, Ne, He or Ar impurities on WC surfaces was carried out by MD and dynamic BCA simulations. The simplified MD simulation set up is shown in Fig. 7, the exact details can be found in **I** and **II**. During the simulations, if an atom or cluster of atoms was no longer bonded to the surface of the sample (either directly or by its neighbor), it was considered sputtered and taken out of the system.

Generally, the C and W sputtering yields, which were obtained by MD, were higher with impurity bombardment than with pure D bombardment. Since WC is a multi-elemental material, the W and C sputtering yields are fluence dependent. The MD yields reported in **I** were averaged over low fluences and did not reach the steady state as illustrated by SDTrimSP calculations in Fig. 8. To obtain reliable MD sputtering yields, further simulations using “steady state” composition as initial sample should be carried out as a separate work.

The key result of **I** is the analysis of the sputtering species and their sputtering mechanism at the considered 100 to 300 eV bombarding energies. Preferential C single atom sputtering was observed. The most striking result was that W was dominantly sputtered as WC dimers or other small W_xC_y

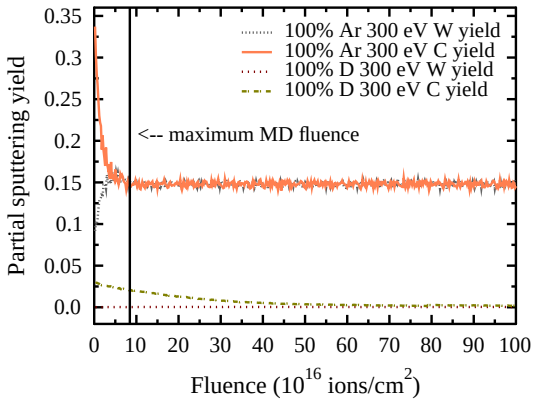

Figure 8: SDTrimSP results for fluence dependent sputtering yields due to preferential sputtering. The maximum fluence obtained by MD is shown as a reference. From publication **I**.

molecules. The complete catalogue of all sputtered species is given in publication **I**. Snapshots of a WC dimer sputtering by a 300 eV Ar impact on a WC surface is shown in Fig. 9. Figure 9 (a) shows the ion shortly before bombarding the surface. In (b) the Ar trajectory in the sample is sketched: it first collides with a C atom near the surface, then there are multiple collisions in the sample, and finally it hits a W atom. In (c)-(e) this W atom pulls the C atom from the surface, and (f) shows the sputtered WC dimer. The latter mechanism was recognized to be similar to the dimer sputtering mechanism at low bombarding energy for Cu reported by Karetta and Urbassek [13]. The difference is that in the simulations in **I** the sputtered dimer consists of two different atom species: C and W. The sputtering is physical at a relative low bombarding energy and multiple collisions are responsible for the dimer sputtering. As in the case of Cu dimer sputtering [13], the majority of the WC dimers were neighbors in the sample before sputtering. However, in some cases a bombarding C ion was sputtered as a WC dimer after multiple collisions. Larger clusters, that were sputtered, originated from nearest neighbor positions on the surface. The WC dimer and cluster/molecule sputtering was almost only seen in impurity bombardment, meaning that the heavier C, W, and noble gas ions were responsible for their sputtering.

5.2 Blistering

Publication **II** investigated D trapping and re-emission, and the structural changes in the sample during the D and impurity bombardment on WC using MD simulations. D bombardment with and without impurities changed in the sample the structure from crystalline to amorphous. The “gradual amorphization” process, shown in snapshots in Fig. 10, has also been observed by Rutherford Backscattering Spectroscopy (RBS) in Si and GaN [84–86]. Since MD does not consider long time

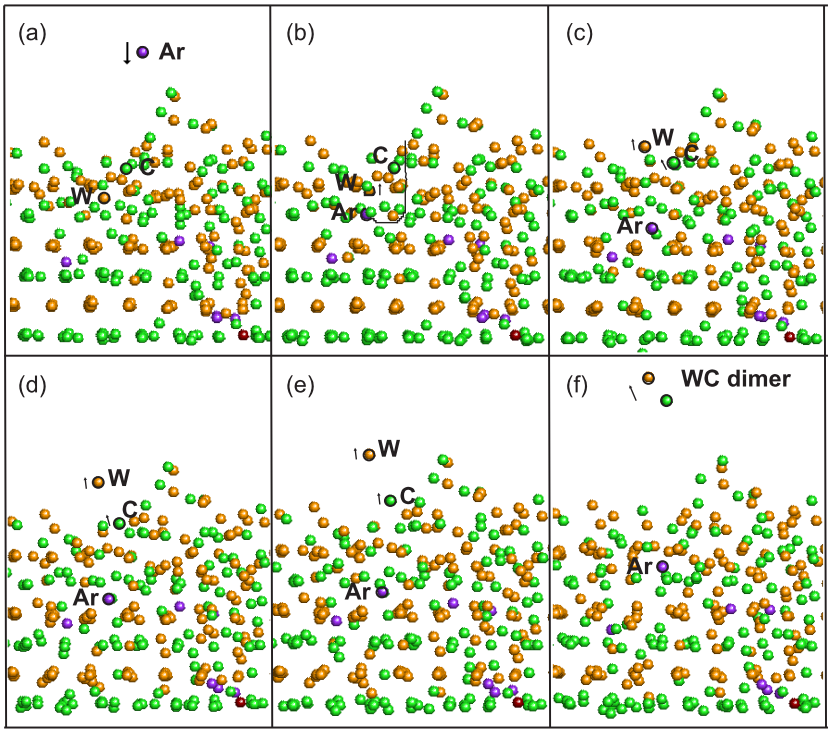

Figure 9: Dimer sputtering mechanism: physical sputtering. (a) 300 eV Ar is bombarded, first hitting a C atom near the surface and leading to multiple collisions in the sample ((b) shows its trajectory) and finally colliding with a W atom. In (c)-(e) this W pulls along the C atom from the surface, and (f) shows the sputtered WC dimer. The arrows indicate in which directions the atoms are moving. Color code: green/very light gray C, orange/light gray W, purple/dark gray Ar, red/very dark gray D (snapshots taken from 90% D 10% Ar with 300 eV on (0001)-W). The figures show the projection of a full three-dimensional cell into a two-dimensional plane. From publication **I**.

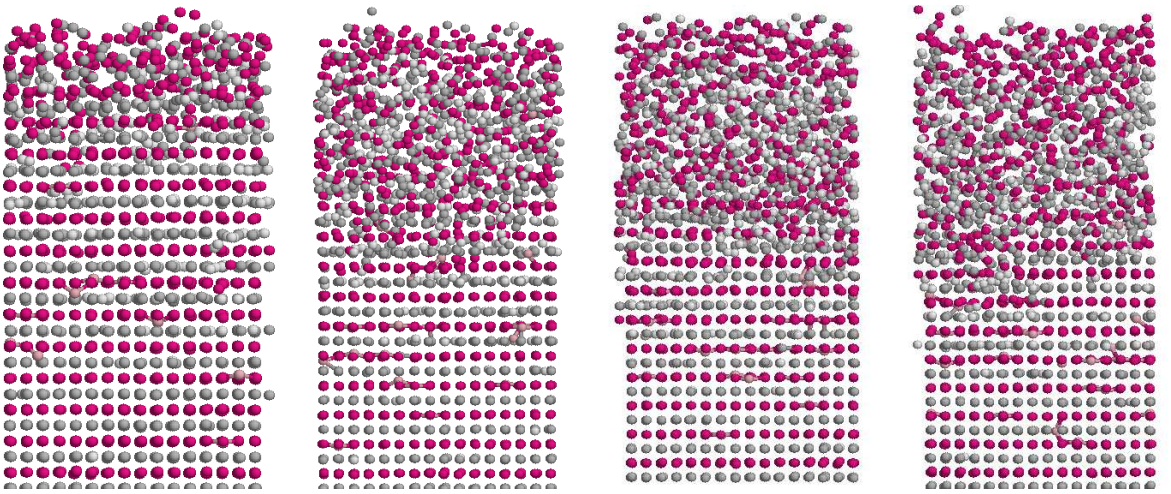

(a) 100 eV, 500 impacts (b) 100 eV, 1000 impacts (c) 100 eV, 1300 impacts (d) 100 eV, 2000 impacts

Figure 10: Snapshots of amorphization of the sample by deuterium bombardment with He impurities on (0001)-W. (a) shows the sample after 500, (b) 1000, (c) 1300, and (d) 2000 ion impacts with 100 eV/ion. The very light gray spheres represent D atoms, the light pink/medium gray He, the dark gray C, and the magenta/very dark gray ones W atoms. The figures show the projection of a full three-dimensional cell into a two-dimensional plane. From publication **II**.

scale diffusion, the MD results are directly relevant for low temperatures or high fluxes, for which no significant defect migration occurs.

The key result of **II** is that D accumulation in WC can lead to a blistering or flaking-like effect, which is illustrated in Fig 11. If a steady-state D concentration in the sample is reached, the force it exerts due to the D_2 gas pressure can lead to a rupture in the sample. This mechanism is the consequence of the high fluxes that were used in the simulations. It is not responsible for blisters seen in experiments on W that are related to diffusion processes and where fluxes are orders of magnitude lower.

D_2 re-emission after annealing from 600 to 1000 K showed that D_2 is highly mobile in WC. Examining the migration path and bonding for 600 K revealed that all re-emitted D_2 existed as molecules in the sample before re-emission. Hence, annealing for longer time-scales than considered here, most D in form of D_2 would leave the sample, and then most of the trapped D would be bonded to C. Thus, the concentration of C in WC determines the amount of trapped D.

Unfortunately, no direct comparison of the MD simulations to experiment is possible, since the MD fluxes were orders of magnitude higher and the fluence much lower than in experiments. However, mixed ion beam experiments on WC using high (experimental) fluxes could validate these results and bring more insight in the mechanisms.

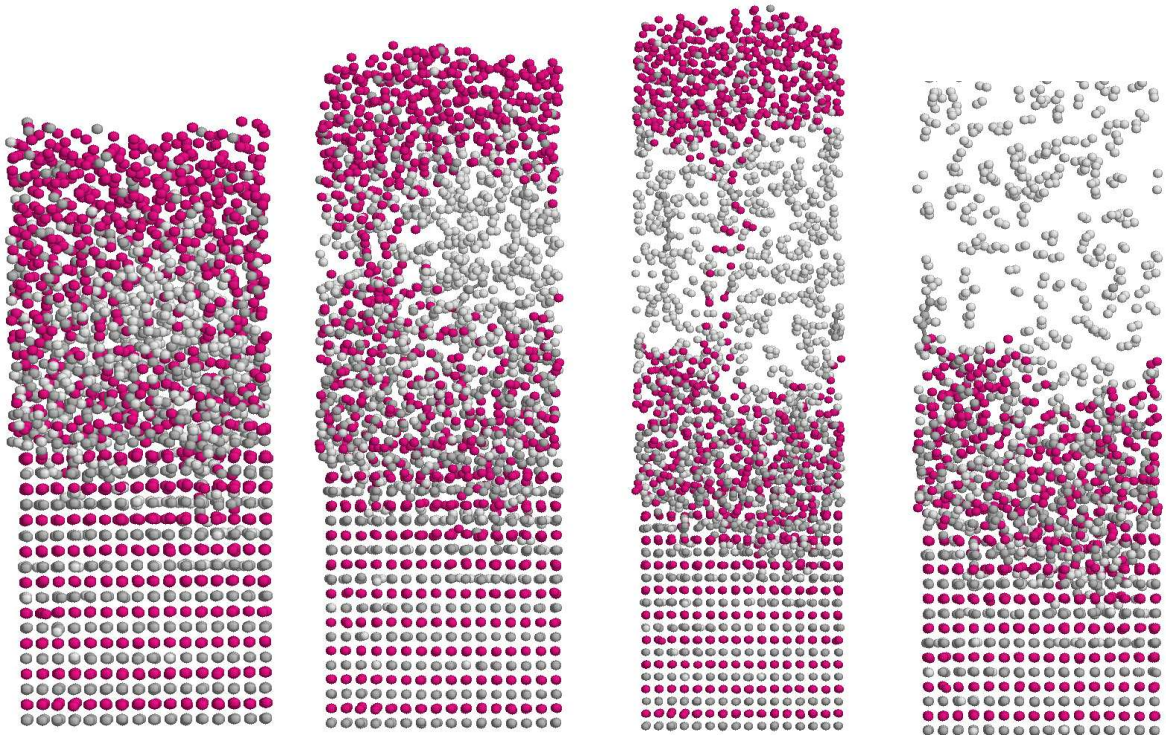

(a) 2500 impacts (b) 3100 impacts (c) 3365 impacts (d) 3373 impacts

Figure 11: Snapshots of D_2 bubble formation (a) after 2500 and (b) 3100 ion impacts with 90% D and 10% W (100 eV/ion) on W-terminated WC. In (c), after 3365 impacts, a separate layer containing D_2 molecules and hydrocarbons is formed (blister). In the following the top of the sample flew off (flaking): (d) after 3373 bombardments. The light gray spheres represent D atoms, the dark gray C, and the magenta/very dark gray ones W atoms. The figures show the projection of a full three-dimensional cell into a two-dimensional plane. From publication **II**.

6 RADIATION EFFECTS IN MODEL ALLOYS OF STEEL

6.1 Single cascade damage

Single displacement cascades using MD were studied in publications **III** and **IV** (random Fe-Cr alloys with 5 and 15% Cr) and **V** (100% Ni and random Fe-40%Ni, Fe-50%Ni and Fe-75%Ni). Multi-elemental effects on the primary damage state were investigated and compared to the damage in 100% Fe.

Snapshots of the time evolution of a single cascade in Fe-5%Cr are shown in Fig. 4, the exact simulation procedure is described in **III**. An Fe atom was used as PKA in all simulations except in pure Ni. The defect production in bcc cells was analyzed using Wigner-Seitz (WS) cells centered at each lattice site: an empty cell corresponded to a vacancy and a cell filled with two atoms to a SIA configuration. For fcc Equivalent Sphere (ES) analysis was used following the same approach as in [87]. Atoms were considered "outside spheres" if they were outside a radius of $r_{ES} = 0.27a_0$ (a_0 is the lattice parameter). Vacancies and SIAs were detected by calculating the imbalance of empty spheres and atoms outside spheres belonging to the same cluster: *i.e.* a cluster consisting of 15 atoms outside spheres and 10 empty spheres was counted as five SIAs.

The main result of **III** is that the variation of the Cr concentration has no effect on the amount of survived Frenkel pairs (Fig 12(a)) in Fe-Cr, nor on the distribution of defects in clusters, as compared to results obtained in pure Fe. Figure 12(b) shows the only noticeable effect of the Cr content on the cascade-induced defects: the enrichment of Cr in survived SIAs, depending on the Cr content, the PKA energy and the potential applied. Moreover, in **IV** it was shown that also the size distribution of SIA clusters is independent of Cr concentration.

In Fe-Ni alloys, independent of Ni concentration, about the same number of FPs was produced. In pure Ni cells the smallest number of FPs was found, although the Ni PKA has a higher mass than the Fe PKA.

6.2 Prolonged irradiation

The purpose of publication **V** was to analyze the effect of prolonged radiation damage neglecting long term diffusion, *i.e.* by the overlapping of single cascades, on the production of defects, their clustering and distribution. The agglomeration of cascades in bcc Fe-Cr and Fe-Ni and fcc Fe-Ni alloys of different Ni and Cr concentrations was investigated in initially random and ordered Ni and Cr distributed crystals.

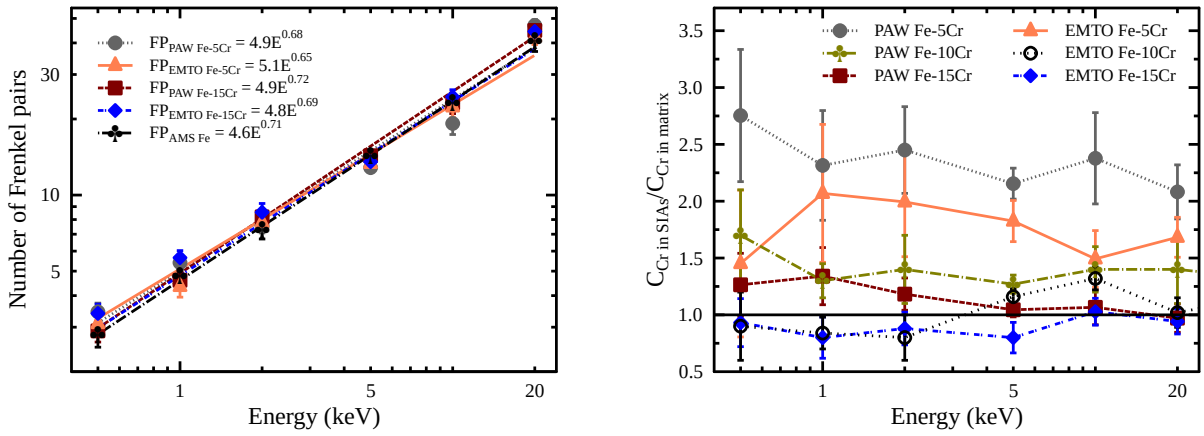

(a) (b)

Figure 12: (a) The average number of surviving Frenkel pairs as a function of recoil damage energy obtained by cascade simulations in Fe-Cr, and in pure Fe using the AMS [78] potential (values from [55]). The parameters A and m for Frenkel pair $FP = A(E_{PKA})^m$ model by Bacon et al. [43] are given as a reference. (b) Ratio of the Cr content in SIAs over the Cr content in the Fe-Cr matrix obtained by cascade simulations. The corresponding values for Fe-10%Cr [55] have been added. The error bars give the 1σ standard error of the average. From publication **III**.

During the simulations, as the number of cascade overlaps increased, stacking fault-tetrahedra (SFT) defects appeared in all fcc cells. SFTs were detected by visually checking for tetrahedral pyramids of empty spheres. An example for a stacking fault tetrahedra is shown in Fig. 13. Appearances of SFTs are noticeable, since they can be experimentally observed.

One main difference in the FP production by increasing number of cascades in the bcc and fcc simulation cells was identified. In all bcc cells, a saturation of the number of FPs was seen (Fig. 14(a)). In the fcc alloys (Fig. 14(b)), the number of FPs was not saturated after 200 cascades and more damage was accumulated in the fcc crystals than in the bcc ones. It was concluded that the more efficient growth of SIA clusters and SFTs in fcc alloys is responsible for the higher damage accumulation. Although the results in **V** are without long time scale diffusion effects, the experimental trend of more loops in fcc than in bcc metals is reproduced [88]. The results confirm that bcc materials are more radiation resistant than fcc ones and are therefore more suitable for nuclear applications from this perspective.

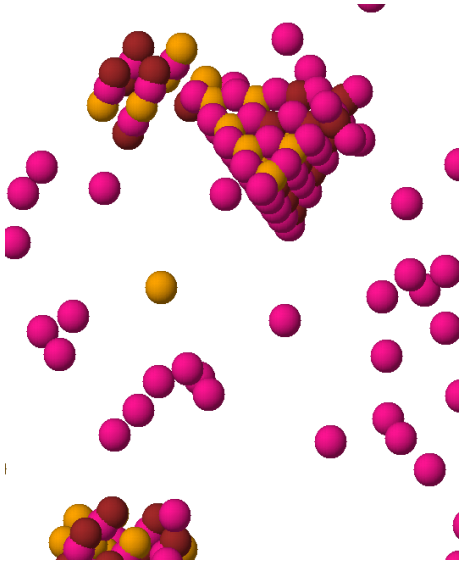

Figure 13: SFT after 160 overlaps in ordered Fe-50%Ni. Color code: magenta/medium gray spheres represent empty spheres, dark red/dark gray spheres Ni atoms and beige/light gray spheres Fe atoms. From publication **V**.

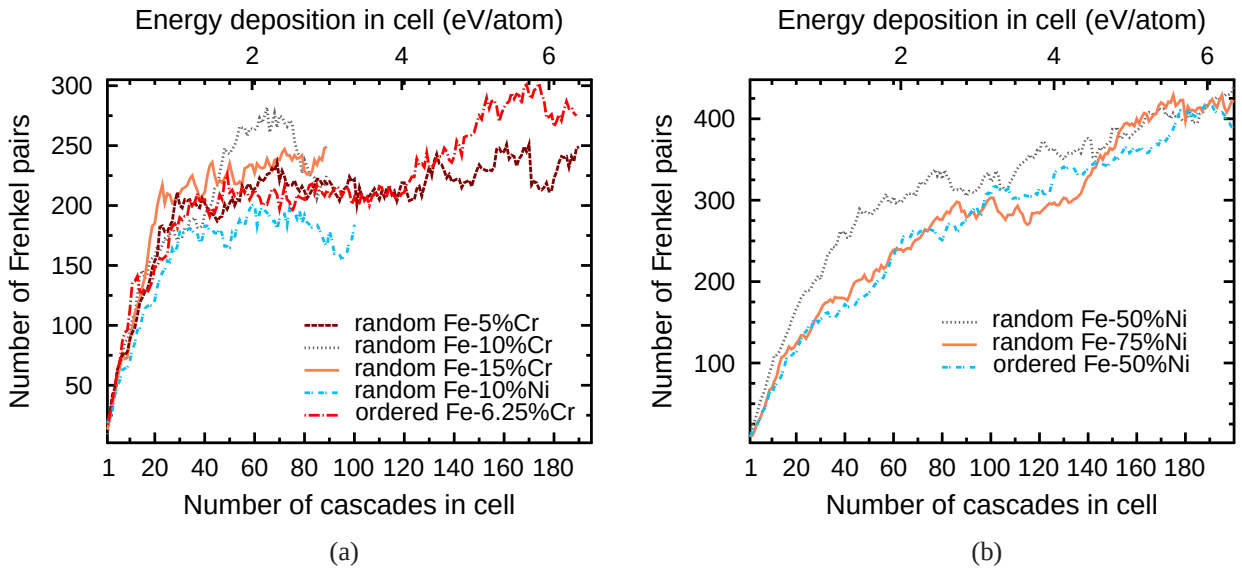

Figure 14: The number of Frenkel pairs depending on the number of cascades in the (a) bcc (Wigner Seitz cell analysis) and (b) fcc cells (equidistant sphere analysis). From publication **V**.

6.3 Changes in chemical order

Changes of Cr or Ni ordering in the Fe matrices was investigated in **III** for single cascades and **V** for overlapping cascades. The ordering was identified by the short range order (SRO) parameters [89] in different nearest neighbor shells. The ordering of Cr or Ni in Fe can be described by the SRO parameter $\alpha^{(i)}_{Cr/Ni}$. It is defined as

$$\alpha^{(i)}_{Cr/Ni} = 1 - \frac{n^i_{Fe}}{m_{Cr/Ni}c^i}, \tag{23}$$

where $m_{Cr/Ni}$ is the Cr or Ni concentration in Fe, i is the number of shell surrounding a Cr or Ni atom with n^i_{Fe} number of Fe atoms, and a total of c^i atoms in that shell. In bcc alloys the averages of first and second shell SRO_{12} and fourth and fifth shell SRO_{45} were calculated as described in **V**.

If the SRO parameter has the same sign in all i shells and is converging to zero, then the SRO parameter can be interpreted as: (i) a tendency for clustering at short range for positive values, and (ii) a tendency for ordering at short range for negative values. If the SRO parameter switches sign in different shells, long range order is observed. The degree of order can be measured experimentally by X-ray or neutron diffraction. It is an important concept in studying irradiation effects in alloys, considering *e.g.* an ordered alloy being disordered by heavy irradiation with nuclear particles at constant temperature [73, 89]

The averaged first and second nearest neighbor SRO for accumulating cascades in the bcc cells is shown in Fig. 15 (a). The trends observed in the figure, *i.e.* Fe-5%Cr becomes more ordered, while in Fe-15%Cr small Cr clusters are formed, and in Fe-10%Cr the alloy stays on average random, agree with the SRO_{12} parameters for single cascades given in **III**. Moreover, the observations are consistent with the interpretation of the SRO parameter in a solid solution with Cr precipitates in Fe-rich Fe-Cr alloys [90]. The results do not contradict the experimentally measured SRO parameters of equilibrium alloys [91, 92]. Unfortunately, direct comparison with the experiments in [91, 92] is not possible, since the conditions are largely different: in publication **V** the atomic redistribution was produced by accumulating damage in a diffusionless system, while in experiments this was achieved by ageing and no guarantee exists that thermodynamic equilibrium was finally reached.

The results in **V** are relevant since they show that the high temperature and possibly the local melting induced by the heat spike of cascades and their agglomeration in the short time scales is enough to form small Cr clusters in Fe-15%Cr, and produce Cr ordering in Fe-5%Cr in initially random Fe-Cr crystals. However, the effect of Cr clustering and ordering is canceled in Fe-10%Cr, which suggests that, at least from the point of view of phase stability, 10% Cr may turn out advantageous for nuclear material applications.

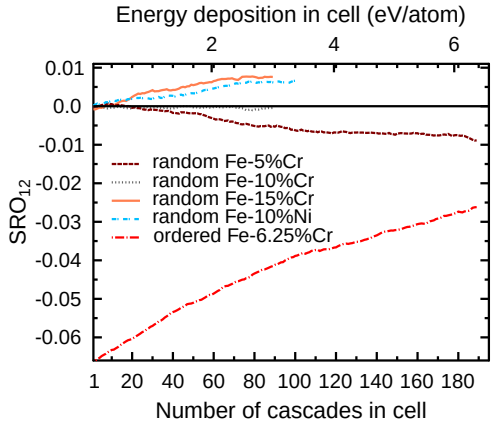

(a)

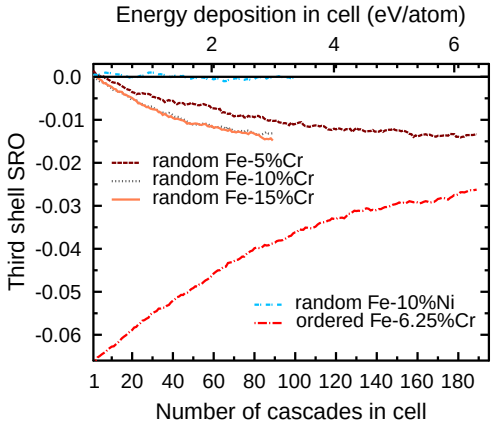

(b)

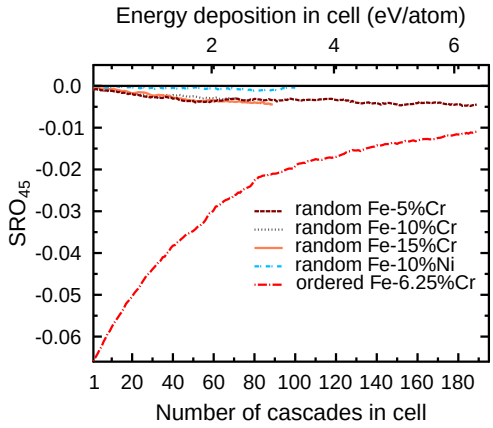

(c)

Figure 15: The change in ordering depending on the number of cascade in bcc cells by (a) the average SRO parameter of 1st and 2nd (b) SRO parameter of 3rd, and (c) in the average SRO of 4th and 5th nearest neighbor shell. From publication **V**.

For Fe-Ni alloys, no clear tendency towards Ni ordering or clustering in the initially random alloys was found in the analysis of the first five nearest neighbor shells in publication **V**. To obtain a reliable conclusion more statistics *e.g.* by running simulations in initially different random cells, would be needed, which was beyond the scope of **V**.

The accumulation of cascades in initially ordered Fe-6.25%Cr and Fe-50%Ni showed an increasing disorder with increasing number of cascade overlaps in the simulation cell. This result agrees with other studies: in Fe-Al alloys disordering in initially ordered fcc cells was also observed experimentally and by MD [93, 94].

7 CONCLUSIONS

In this thesis, microscopic radiation effects in multi-elemental fusion reactor materials were studied by molecular dynamics and dynamic binary collision approximation simulations. Prolonged radiation effects were investigated on WC, which will be formed at the divertor of ITER, and in Fe-Cr and Fe-Ni alloys, which are model materials for the structural steel.

The microscopic effects of D bombardment on WC surfaces, *e.g.* the catalogue of sputtering species, or the microscopic primary radiation damage profiles in Fe-Cr or Fe-Ni alloys are included into data bases. These data bases are used in multiscale modelling, which has the aim to investigate how these microscopic effects are connected to the macroscopic degradation of materials under irradiation. Answering that question is crucial for the scientific and engineering approaches in developing advanced fusion reactor materials.

The results of deuterium bombardment (publications **I** and **II**) on WC are relevant, since they show that physical sputtering of WC molecules or clusters is possible, and that microscale blisters may form on WC surfaces under high flux irradiation conditions.

Moreover, the results for single cascades (**III** to **V**), showing that there are hardly any multi-elemental effects of Fe-Cr and Fe-Ni on the primary damage state by cascades in comparison to pure Fe, are significant, since they show that the large existing data bases for Fe can be applied also for these alloys.

This thesis is therefore a meaningful contribution to the multiscale modelling efforts within the EFDA and Getmat projects.

ACKNOWLEDGMENTS

I thank the heads of the Department of Physics, Prof. Juhani Keinonen, and the Materials Physics Division, Prof. Jyrki Räisänen, for the opportunity and the facilities to conduct my PhD studies at the University of Helsinki.

For his encouragement and guidance throughout the work for this thesis I wish to thank Prof. Kai Nordlund. I appreciate his easy approach to discuss science, and although having lots of other obligations, trying to be the best supervisor. He has been very generous with opportunities and funds to meet other researchers on conferences and workshops.

I would like to thank my former colleagues in the lab, Dr. Carolina Björkas and Dr. Niklas Juslin, for their contributions to the publications included in this thesis. I am also grateful to my collaborators at SCK-CEN, Belgium, Dr. Lorenzo Malerba, Dr. Dmitry Terentyev, and Dr. Giovanni Bonny for their advise and fruitful discussions.

For writing the dissertation manuscript, I want to acknowledge the constructive criticism by Dr. Kalle Heinola and Dr. Olli Pakarinen.

For the years of working in the lab, I want to thank my friends and co-workers for the many adventures and culture shocks. Especially thankful I am to those, who were encouraging me to practice the Finnish language (and Swedish, too ;).

My warmest thanks to my family for the support to any strange idea I ever had - like living in Finland.

This thesis work received funding by the European Communities under the contract of Association between EURATOM-Tekes, and was carried out within the framework of the European Fusion Development Agreement. This work has also received partial funding from EURATOM's 7th Framework Programme (FP7/2007-2011) under grant agreement number 212175 (GetMat project). It was performed within the Finnish Centre of Excellence in Computational Molecular Science (CMS), financed by the Academy of Finland and the University of Helsinki. Personal grants by the National Graduate School in Materials Physics, the Vilho, Yrjö and Kalle Väisälä Foundation, and the Chancellor's Travel Grant are gratefully acknowledged.

Helsinki, October 2011
Katharina Vörtler

References

1. J. Wesson, *Tokamaks*, 2nd ed. (Clarendon Press, Oxford, UK, 1997).

2. European Fusion Development Agreement (EFDA), *http://www.efda.org*.

3. P. Träskelin, *Sticking and erosion at carbon-containing plasma-facing materials in fusion reactors*, Ph.D. thesis, University of Helsinki, 2006.

4. N. Juslin, *Computer simulation of H and He effects in fusion reactor materials*, Ph.D. thesis, University of Helsinki, 2009.

5. C. Björkas, *Interatomic potentials for fusion reactor material simulations*, Ph.D. thesis, University of Helsinki, 2009.

6. K. Heinola, *Multiscale study on hydrogen mobility in metallic fusion divertor material*, Ph.D. thesis, University of Helsinki, 2010.

7. The ITER organisation, *http://www.iter.org*.

8. The European Atomic Energy Community (EURATOM), *http://www.euratom.org*.

9. *Kernfusion - Berichte aus der Forschung, Folge 2*, Max-Planck-Institut für Plasmaphysik (IPP), 2002, online available at *http://www.ipp.mpg.de/ippcms/de/pr/publikationen/pdf/berichte.pdf*.

10. C. Linsmeier, J. Luthin, and P. Goldstraß, *Mixed material formation and erosion*, J. Nucl. Mater. **290-293**, 25 (2001).

11. R. P. Doerner, *The implications of mixed-material plasma-facing surfaces in ITER*, J. Nucl. Mater. **363**, 32 (2007).

12. R. Behrisch and W. Eckstein (ed.), *Sputtering by Particle Bombardment: Experiments and Computer Calculations from Threshold to Mev Energies* (Springer, Berlin, 2007).

13. F. Karetta and H. M. Urbassek, *The Dimer Sputtering Mechanism of Cu(001) at Low Bombarding Energy*, Appl. Phys. A **55**, 364 (1992).

14. J. Samela and K. Nordlund, *Dynamics of cluster induced sputtering in gold*, Nucl. Instr. Meth. Phys. Res. B **263**, 375 (2007).

15. E. Salonen, K. Nordlund, J. Keinonen, and C. H. Wu, *Swift chemical sputtering of amorphous hydrogenated carbon*, Phys. Rev. B **63**, 195415 (2001).

16. J. Roth, B. M. U. Scherzer, R. S. Blewer, D. K. Brice, S. T. Picraux, and W. R. Wampler, *Trapping, detrapping and replacement of keV hydrogen implanted into graphite*, J. Nucl. Mater. **93 & 94**, 601 (1980).

17. E. Salonen, *Overview of the atomistic modeling of the chemical erosion of carbon*, Physica Scripta **T111**, 133 (2004).

18. E. de Juan Pardo, M. Balden, B. Cieciwa, C. Garcia-Rosales, and J. Roth, *Erosion Processes of Carbon Materials under Hydrogen Bombardment and their Mitigation b*, Physica Scripta **T111**, 62 (2004).

19. P. S. Krstic, C. O. Reinhold, and S. Stuart, *Chemical sputtering from amorphous carbon under bombardment by deuterium atoms and molecules*, New J. Phys. **9**, 209 (2007).

20. G. Federici and C. H. Wu, *Modelling of the interaction of hydrogen plasma with amorphous carbon films redeposited in fusion devices*, J. Nucl. Mater. **207**, 62 (1993), and references therein.

21. P. Träskelin, K. Nordlund, and J. Keinonen, *H, He, Ne, Ar-bombardment of amorphous hydrocarbon structures*, J. Nucl. Mater **357**, 1 (2006).

22. C. Hopf, A. von Keudell, and W. Jacob, *Chemical sputtering of hydrocarbon films by low-energy Ar+ ion and H atom impact*, Nucl. Fusion **42**, L27 (2002).

23. H. Plank and W. Eckstein, *Preferential sputtering of carbides under deuterium irradiation - a comparison between experiment and computer simulation*, Nucl. Instr. Meth. Phys. Res. B **124**, 23 (1997).

24. M. I. Guseva, A. L. Suvorov, S. N. Korshunov, and N. E. Lazarev, *Sputtering of beryllium, tungsten, tungsten oxide and mixed W-C layers by deuterium ions in the near threshold energy range*, J. Nucl. Mater. **266-269**, 222 (1999).

25. M. Taniguchi, K. Sato, K. Ezato, K. Yokoyama, M. Dairaku, and M. Akiba, *Sputtering of carbon-tungsten mixed materials by low energy deuterium*, J. Nucl. Mater. **313-316**, 360 (2003).

26. I. Bizyukov, K. Krieger, N. Azarenkov, C. Linsmeier, and S. Levchuk, *Tungsten sputtering and accumulation of implanted carbon and deuterium by simultaneous bombardment with D and C ions*, J. Nucl. Mater. **363-365**, 1184 (2007).

27. W. Eckstein and J. P. Biersack, *Computer Simulation of Two-Component Target Sputtering*, Appl. Phys. A **37**, 95 (1985).

28. P. Träskelin, N. Juslin, P. Erhart, and K. Nordlund, *Hydrogen bombardment simulations of tungsten-carbide surfaces*, Phys. Rev. B **75**, 174113 (2007).

29. J. B. Condon and T. Schober, *Hydrogen bubbles in metals*, J. Nucl. Mater. **207**, 1 (1993).

30. O. Ogorodnikova, J. Roth, and M. Mayer, *Deuterium retention in tungsten in dependence of the surface conditions*, J. Nucl. Mater. **313-316**, 469 (2003).

31. N. Enomoto, S. Muto, T. Tanabe, J. Davis, and A. Haasz, *Grazing-incidence electron microscopy of surface blisters in single- and polycrystalline tungsten formed by H+, D+ and He+ irradiation*, J. Nucl. Mater. **385**, 606 (2009).

32. T. Shimada, Y. Ueda, and M. Nishikawa, *Mechanism of blister formation on tungsten surface*, Fusion Engineering and Design **66-68**, 247 (2003).

33. V. Alimov, J. Roth, R. Causey, D. Komarov, C. Linsmeier, A. Wiltner, F. Kost, and S. Lindig, *Deuterium retention in tungsten exposed to low-energy, high-flux clean and carbon-seeded deuterium plasmas*, Journal of Nuclear Materials **375**, 192 (2008).

34. M. Fukumoto, Y. Ohtsuka, Y. Ueda, M. Taniguchi, M. Kashiwagi, T. Inoue, and K. Sakamoto, *Blister formation on tungsten damaged by high energy particle irradiation*, Journal of Nuclear Materials **375**, 224 (2008).

35. W. Shu, A. Kawasuso, and T. Yamanishi, *Recent findings on blistering and deuterium retention in tungsten exposed to high-fluence deuterium plasma*, Journal of Nuclear Materials **386-388**, 356 (2009).

36. V. Alimov and D. Komarov, *Deuterium retention in carbon and tungsten-carbon mixed films deposited by magnetron sputtering in D2 atmosphere*, J. Nucl. Mater. **313-316**, 599 (2003).

37. V. Alimov, *Deuterium retention in pure and mixed plasma facing materials*, Physica Scripta **T108**, 46 (2004).

38. E. Igarashi, Y. Nishikawa, T. Nakahata, A. Yoshikawa, M. Oyaidzu, Y. Oya, and K. Okuno, *Dependence of implantation temperature on chemical behavior of energetic deuterium implanted into tungsten carbide*, J. Nucl. Mater. **363-365**, 910 (2007).

39. J. A. Brinkman, *On Nature of Radiation Damage in Metals*, J. App. Phys **25**, 961 (1953).

40. C.-Y. Wei, M. I. Current, and D. N. Seidman, *Direct observation of the primary state of damage of ion-irradiated tungsten*, Philosophical Magazine A **44**, 459 (1981).

41. D. N. Seidman, M. I. Current, P. Pramanik, and C.-Y. Wei, *Direct observations of the primary damage state of radiation damage of ion-irradiated tungsten and platinum*, Nuclear Instruments and Methods **182**, 477 (1981).

42. D. J. Bacon and T. Diaz de la Rubia, *Molecular dynamics computer simulations of displacement cascades in metals*, Journal of Nuclear Materials **216**, 275 (1994).

43. D. J. Bacon, A. F. Calder, F. Gao, V. G. Kapinos, and S. J. Wooding, *Computer simulation of defect production by displacement cascades in metals*, Nucl. Instr. and Meth. in Phys. Res. B **102**, 37 (1995).

44. D. J. Bacon, A. F. Calder, and F. Gao, *Defect production due to displacement cascades in metals as revealed by computer simulation*, Journal of Nuclear Materials **251**, 1 (1997).

45. R. S. Averback and T. Diaz de la Rubia, in *Solid State Physics*, edited by H. Ehrenfest and F. Spaepen (Academic Press, New York, 1998), Vol. 51, pp. 281–402.

46. K. Nordlund, M. Ghaly, R. S. Averback, M. Caturla, T. Diaz de la Rubia, and J. Tarus, *Defect production in collision cascades in elemental semiconductors and FCC metals*, Phys. Rev. B **57**, 7556 (1998).

47. A. Seeger, in *Proc. 2nd UN Int. Conf. on Peaceful Uses of Atomic Energy*, United nations, New York (United nations publication, Geneva, 1958), Vol. 6, p. 20.

48. R. Kemp, *Introduction to fusion power plant materials*, , Department of Materials Science and Metallurgy, University of Cambridge, 2006, online available at http://www.msm.cam.ac.uk/phase-trans/2006/Irradiated_Steel/Irradiated_Steel.html.

49. L. Mansur, *Theory and experimental background on dimensional changes in irradiated alloys*, J. Nucl. Mater. **216**, 97 (1994).

50. L. Malerba, *Molecular dynamics simulation of displacement cascades in α-Fe: A critical review*, J. Nucl. Mater. **351**, 28 (2006).

51. A. F. Calder and D. J. Bacon, *Computer simulation study of the effects of copper solutes on cascade damage in FeCu alloys*, Mat. Res. Soc. Symp. **439**, 521 (1997).

52. A. F. Calder, D. J. Bacon, A. V. Barashev, and Y. N. Osetsky, *Effect of mass on the primary knock-on atom on displacement cascade debris in alpha-iron*, Phil. Mag. Lett. **88**, 43 (2008).

53. C. S. Becquart, C. Domain, J. C. Van Duysen, and J. M. Raulot, *The role of Cu in displacement cascades examined by molecular dynamics*, J. Nucl. Mater. **294**, 274 (2001).

54. D. Terentyev, L. Malerba, R. Chakarova, C. Domain, K. Nordlund, P. Olsson, M. Rieth, and J. Wallenius, *Displacement cascades in Fe-Cr: a molecular dynamics study*, J. Nucl. Mater. **349**, 119 (2006).

55. C. Björkas, K. Nordlund, L. Malerba, D. Terentyev, and P. Olsson, *Simulation of displacement cascades in $Fe_{90}Cr_{10}$ using a two band model potential*, J. Nucl. Mater. **372**, 312 (2008).

56. L. Malerba, D. Terentyev, P. Olsson, R. Chakarova, and J. Wallenius, *Molecular dynamics simulation of displacement cascades in Fe-Cr alloys*, J. Nucl. Mater. **329–333**, 1156 (2004).

57. J.-H. Shim, H.-J. Lee, and B. D. Wirth, *Molecular dynamics simulation of primary irradiation defect formation in Fe-Cr alloys*, J. Nucl. Mater. **351**, 56 (2006).

58. J. Wallenius, P. Olsson, C. Lagerstedt, N. Sandberg, R. Chakarova, and V. Pontikis, *Modelling of Chromium precipitation in Fe-Cr alloys*, Phys. Rev. B **69**, 094103 (2003).

59. G. Bonny, R. C. Pasianot, and L. Malerba, *Fe-Ni many-body potential for metallurgical applications*, Model. Simul. Mater. Sci. Eng. **17**, 025010 (2009).

60. J. F. Ziegler, J. P. Biersack, and U. Littmark, *The Stopping and Range of Ions in Matter* (Pergamon, New York, 1985).

61. W. Eckstein, R. Dohmen, A. Mutzke, and R. Schneider, in *SDTrimSP: Ein Monte-Carlo Code zur Berechnung von Stossereignissen in ungeordneten Targets = SDTrimSP: A Monte Carlo Code for Calculating Collision Phenomena in Randomized Targets* (Max-Planck-Institut für Plasmaphysik, Greifswald, Germany, 2007).

62. G. W. Gear, *Numerical initial value problems in ordinary differential equations* (Prentice-Hall, Englewood Cliffs, NJ, USA, 1971).

63. K. Nordlund, 2006, PARCAS computer code. The main principles of the molecular dynamics algorithms are presented in [46, 95]. The adaptive time step and electronic stopping algorithms are the same as in [64].

64. K. Nordlund, *Molecular dynamics simulation of ion ranges in the 1 – 100 keV energy range*, Comput. Mater. Sci. **3**, 448 (1995).

65. K. Nordlund, *Introduction to atomistic simulations*, lecture notes.

66. M. P. Allen and D. J. Tildesley, *Computer Simulation of Liquids* (Oxford University Press, Oxford, England, 1989).

67. H. J. C. Berendsen, J. P. M. Postma, W. F. van Gunsteren, A. DiNola, and J. R. Haak, *Molecular dynamics with coupling to external bath*, J. Chem. Phys. **81**, 3684 (1984).

68. K. Albe, K. Nordlund, and R. S. Averback, *Modeling metal-semiconductor interaction: Analytical bond-order potential for platinum-carbon*, Phys. Rev. B **65**, 195124 (2002).

69. G. C. Abell, *Empirical chemical pseudopotential theory of molecular and metallic bonding*, Phys. Rev. B **31**, 6184 (1985).

70. J. Tersoff, *New empirical approach for the structure and energy of covalent systems*, Phys. Rev. B **37**, 6991 (1988).

71. D. W. Brenner, *Empirical potential for hydrocarbons for use in simulating the chemical vapor deposition of diamond films*, Phys. Rev. B **42**, 9458 (1990).

72. N. Juslin, P. Erhart, P. Träskelin, J. Nord, K. O. E. Henriksson, K. Nordlund, E. Salonen, and K. Albe, *Analytical interatomic potential for modelling non-equilibrium processes in the W-C-H system*, J. Appl. Phys. **98**, 123520 (2005).

73. C. Kittel, *Introduction to Solid State Physics*, fourth ed. (John Wily & Sons, Inc., New York, USA, 1971).

74. M. S. Daw and M. I. Baskes, *Embedded-atom method: Derivation and application to impurities, surfaces, and other defects in metals*, Phys. Rev. B **29**, 6443 (1984).

75. S. L. Dudarev and P. M. Derlet, *A magnetic interatomic potential for molecular dynamics simulations*, J. Phys.: Condens. Matter **17**, 1 (2005).

76. P. Olsson, J. Wallenius, C. Domain, K. Nordlund, and L. Malerba, *Two-band model of* α*-prime phase formation in Fe-Cr.*, Phys. Rev. B **72**, 214119 (2005).

77. G. J. Ackland and S. K. Reed, *Two-band second moment model and an interatomic potential for caesium*, Phys. Rev. B **67**, 174108 (2003).

78. G. J. Ackland, M. I. Mendelev, D. J. Srolovitz, S. Han, and A. V. Barashev, *Development of an interatomic potential for phosphorus impurities in alpha -iron*, J. Phys. Condens. Matter **16**, S2629 (2004).

79. A. Voter and S. P. Chen, *Accurate interatomic potentials for Ni, Al and Ni_3Al*, Mat. Res. Soc. Symp. Proc. **82**, 175 (1989).

80. O. K. Andersen and T. Saha-Dasgupta, *Muffin-tin orbitals of arbitrary order*, Phys. Rev. B **62**, R16219 (2000).

81. G. Kresse and D. Joubert, *From ultrasoft pseudopotentials to the projector augmented-wave method*, Phys. Rev. B **59**, 1758 (1999).

82. P. Blöchl, *Projector augmented-wave method*, Phys. Rev. B **50**, 17953 (1994).

83. M. S. Daw, S. M. Foiles, and M. I. Baskes, *The embedded-atom method: a review of theory and applications*, Mat. Sci. Rep. **9**, 251 (1993).

84. T. Lohner, E. Kótai, N. Khánh, Z. Tóth, M. Fried, K. Vedam, N. Nguyen, L. Hanekamp, and A. van Silfhout, *Ion-implantation induced anomalous surface amorphization in silicon*, Nuclear Instruments and Methods in Physics Research Section B: Beam Interactions with Materials and Atoms **85**, 335 (1994).

85. S. Kucheyev, J. Williams, C. Jagadish, J. Zou, and G. Li, *Damage buildup in GaN under ion bombardment*, Phys. Rev. B **62**, 7510 (2000).

86. K. Nakajima, H. Toyofuku, and K. Kimura, *Anomalous Surface Amorphization of Si(001) Induced by 3–5 keV Ar^+ Ion Bombardment*, Japanese Journal of Applied Physics **40**, 2119 (2001).

87. R. E. Voskoboinikov, Y. N. Osetsky, and D. J. Bacon, *Computer simulation of primary damage creation in displacement cascades in copper. I. Defect creation and cluster statistics*, J. Nucl. Mater. **377**, 385 (2008).

88. B. N. Singh and J. H. Evans, *Significant differences in defect accumulation behaviour between fcc and bcc crystals under cascade damage conditions*, J. Nucl. Mater. **226**, 277 (1995).

89. J. M. Cowley, *An Approximate Theory of Order in Alloys*, Phys. Rev. **77**, 669 (1950).

90. P. Erhart, A. Caro, M. S. de Caro, and B. Sadigh, *Short-range order and precipitation in Fe-rich Fe-Cr alloys: Atomistic off-lattice Monte Carlo simulations*, Phys. Rev. B **77**, 134206 (2008).

91. I. Mirebeau, M. Hennion, and G. Parette, *First Measurement of Short-Range-Order Inversion as a Function of Concentration in a Transition Alloy*, Phys. Rev. Lett **53**, 687 (1984).

92. I. Mirebeau and G. Parette, *Neutron study of the short range order inversion in $Fe_{1-x}Cr_x$*, Phys. Rev. B **82**, 104203 (2010).

93. C. Abromeit, H. Wollenberger, S. Matsumura, and C. Kinoshita, *Stability of ordered phases under irradiation*, J. Nucl. Mater. **276**, 104 (2000).

94. G. Schmitz, J. Ewert, F. Harbsmeier, M. Uhrmacher, and F. Haider, *Phase stability of decomposed Ni-Al alloys under ion irradiation*, Phys. Rev. B **63**, 224113 (2001).

95. M. Ghaly, K. Nordlund, and R. S. Averback, *Molecular dynamics investigations of surface damage produced by keV self-bombardment of solids*, Phil. Mag. A **79**, 795 (1999).